Progress In Electromagnetics Research, Vol. 140, 43–62, 2013

SPARSE AUTOFOCUS RECOVERY FOR UNDER-SAMPLED LINEAR ARRAY SAR 3-D IMAGING

Shun-Jun Wei[*] **and Xiao-Ling Zhang**

School of Electronic Engineering, University of Electronic Science and Technology of China, Chengdu 611731, China

Abstract—Linear array synthetic aperture radar (LASAR) is a promising radar 3-D imaging technique. In this paper, we address the problem of sparse recovery of LASAR image from under-sampled and phase errors interrupted echo data. It is shown that the unknown LASAR image and the nuisance phase errors can be constructed as a bilinear measurement model, and then the under-sampled LASAR imaging with phase errors can be mathematically transferred into sparse signal recovery by solving an ill-conditioned constant modulus linear program (ICCMLP) problem. Exploiting the prior sparse spatial feature of the observed targets, a new super-resolution sparse autofocus recovery algorithm is proposed for under-sampled LASAR 3-D imaging. The algorithm is an iterative minimize estimation procedure, wherein it converts the ICCMLP into two independent convex optimal problems, and joints ℓ_1-norm reweights least square regularization and semi-definite relax technique to find the optimal solutions. Simulated and experimental results confirm that the proposed method outperforms the classical autofocus techniques in under-sampled LASAR imaging.

1. INTRODUCTION

High resolution three-dimensional (3-D) imaging is one of the most important abilities of synthetic aperture radar (SAR). As a novel SAR architecture, linear array SAR (LASAR) 3-D imaging has attracted a lot of attentions in the radar community recently [1–5]. Exploiting high resolution 3-D images, LASAR can provide more details in target recognition and decision-making tasks than conventional two-dimensional (2-D) SAR. In addition, unlike classical SAR structures

---

Received 6 February 2013, Accepted 25 April 2013, Scheduled 22 May 2013

[*] Corresponding author: Shun-Jun Wei (grinwshj@163.com).

limited by the side-looking configuration [6, 7], LASAR can work in flexible mode, e.g., forward-looking and down-looking, make it very suitable for the reconnaissance and surveying applications in complex terrains. With the linear array antenna (LAA), LASAR extends the synthetic aperture principle into the cross-track direction (the third dimension) for 3-D imaging. However, in the airborne or spaceborne case, the huge cost of a real full-sampled LAA in tens of meters makes it infeasible to be implemented in practice [8]. Although the multiple-input-multiple-output (MIMO) technique [9–11] can achieve a virtual full-sampled LAA with few transmitter/receiver antennas, there are still some serious drawbacks for LASAR widely applied with such a full-sampled virtual LAA, i.e., large-scale echoes need to be stored, transferred and processed. To further reduce the cost of LASAR data acquisition and processing, one can employ only a few sparse LAA elements at every footprint. We call such an under-sampled system as "sparse-activate" LASAR (SA-LASAR). Based on the synthetic aperture principle and beam-forming, we have developed a ground-based SA-LASAR experimental system [1, 12–14]. The system controls the transmitter/receiver antennas moving on a specific trajectory to synthesize the desired sparse virtual 2-D antenna array. In addition, we also proposed a modified back-projection algorithm (BPA) based on the classical matched filter (MF) theory to form the SA-LASAR 3-D images [12]. However, if the LAA is not dense enough, BPA images may suffer from serious degradation, such as high sidelobes and low resolution.

Based on the observation that typical underlying 3-D terrains usually exhibit strong spatial sparsity (e.g., no scatterer in the atmosphere and the non-penetrating areas), we can formulate the SA-LASAR imaging as a sparse signal recovery problem. Recently compressed sensing (CS) sparse recovery theory has been widely discussed in radar imaging [15–21]. Some effective sparse recovery approaches have also been successfully developed for SAR imaging [22–24], offering many advantages such as super-resolution, sidelobe and speckle suppression, and feature enhancement, etc. In previous work [25], we presented a CS-based sparse recovery approach for LASAR 3-D imaging. But we assumed that the observed signal model of LASAR was exactly known in advance. In practice, due to some inevitable measurement errors during LASAR data acquisition, e.g., the platform motion uncertainty, the LAA jitter and the time synchronization offsets, etc., the LASAR echoes always contain serious phase errors. Although INS/GPS assisted data can be used to achieve coarse correction, some residual phase errors are still remaining. If these residual phase errors are not compensated, CS recovery performance will degrade substantially (such as defocus, spatial distortion and artifacts). Nevertheless, phase errors are seldom taken into account for most existing CS-based SAR imaging. Although various autofocus algorithms have been presented for SAR phase errors correction, e.g., phase gradient autofocus (PGA) algorithm [26], multichannel autofocus (MCA) algorithm [27] and maximum likelihood autofocus (MLA) algorithm [28], etc., most of them are based on post-processing of the conventional fully-samples SAR image. In the case of SA-SAR, as the LAA is not full-sampled, these classical autofocus algorithms may suffer from significant performance loss. These motivate development of a more effective LASAR 3-D autofocus imaging method under the case of under-sampled data. Recently some works were proposed for classical SAR sparse imaging with phase errors [29, 30]. These approaches estimate the phase errors from SAR echoes by a direct calculation method, which assumes that an exactly solution of the sparse signal is obtained in each iteration. However, such an assumption may fail due to the noise interference.

In this paper, to address the issues of SA-LASAR imaging with under-sampled and phase errors corrupted data, we propose a new sparse autofocus recovery algorithm for SA-LASAR 3-D imaging. In the scheme, the SA-LASAR sparse imaging with unknown phase errors is mathematically converted into signal recovery for an ill-conditioned constant modulus linear program (ICCMLP) problem. To find the optimal resolution, the ICCMLP is divided into two independent convex optimal programs, and the estimation is realized by solving an iterative minimization procedure jointing ℓ_1-norm reweights least square regularization with semi-definite relax method. As a result, by exploiting of the sparsity prior, the proposed algorithm provides high resolution capability under the sparse LAA. Simulation and experimental results are used to demonstrate the performance of the proposed approach by various metrics.

The rest of this paper is constructed as follows. In Section 2, we introduce the SA-LASAR signal model and sketch its image formation as a linear inverse problem with the unknown scattering coefficients and phase errors. In Section 3, the sparse autofocus algorithm is proposed and its full steps are discussed. Simulated and experimental results are presented in Section 4 along with the performance analysis. Conclusions are provided in Section 5.

2. SIGNAL MODEL AND PROBLEM FORMULATION

2.1. SA-LASAR Signal Model

The geometric model of SA-LASAR is illustrated in Figure 1. Since the observed 3-D scene is sparse, in each pulse recurrence interval (PRI), only sparse LAA elements are active. According to CS theory, the required LAA element number N_A in SA-LASAR depends on both the scene grids number and the sparity of targets. CS indicates that a K-sparse signal can be exactly reconstructed with $N_0 \geq \mathcal{O}(K \log(M_0/K))$, where N_0 and M_0 are the dimension of the measurement signal and the reconstructed signal respectively. In practice, many numerical experiments also suggest that most K-sparse signals can be recovered exactly once $N_0 \geq 3K$. As mentioned in Section 1, the observed 3-D terrains in LASAR imaging usually exhibit strong sparsity, e.g., in most case K/M_0 is lower than 0.1, so only $N_0 \geq 0.3M_0$ is required in the SA-LASAR system for CS sparse imaging. In this case, the required number of sparse LAA elements is much smaller than that of the conventional full-sampled LAA. These antenna phase center (APC) positions in one synthetic aperture length are described by a position set $\mathbf{P}_A$.

$$\mathbf{P}_A = \{\mathbf{P}_{An} \,|\mathbf{P}_{An} = \langle x_n, y_n, z_n\rangle \,; n \in \Upsilon\,\} \tag{1}$$

where Υ denotes an index set, $\Upsilon = \{1, 2, \ldots, N\}$, and N denotes the total APCs number. The sparse LAA can be a real array antenna or a virtual array antenna synthesized from the synthetic aperture techniques. Assume that the observed targets are all point-like scatterers, the underlying scene can be approximated by discrete

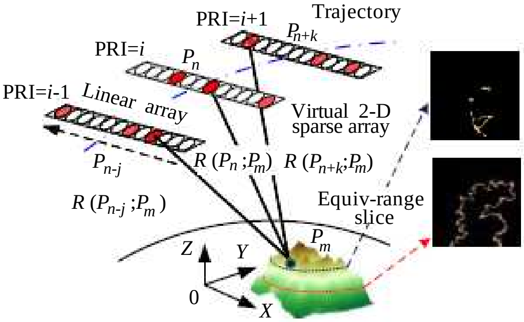

Figure 1. The geometric model of SA-LASAR imaging.

cells, whose positions and scattering coefficients are described as,

$$\mathbf{P}_S = \{\mathbf{P}_{Sm} \,|\mathbf{P}_{Sm} = \langle x_m, y_m, z_m \rangle \,;\ m \in \Omega\} \tag{2}$$

$$\boldsymbol{\sigma} = \{\sigma_m \,|\sigma_m \in \mathbb{C};\ m \in \Omega\} \tag{3}$$

where $\Omega = \{1, 2, \ldots, M\}$, M denotes the total number of the discrete observed scene cells. The slant range from the mth scatterer with position $\mathbf{P}_{Sm}$ to the nth APC with position $\mathbf{P}_{An}$ is $R(\mathbf{P}_{An}; \mathbf{P}_{Sm}) = \|\mathbf{P}_{An} - \mathbf{P}_{Sm}\|_2$, $m = 1, \ldots, M$, $n = 1, \ldots, N$, where $\| \cdot \|_2$ denotes the 2-norm of vector.

Suppose that the sensors transmit a linear frequency modulation (LFM) signal, then, the echo of the scatterer $\mathbf{P}_{Sm}$ can be expressed as

$$s(t, \mathbf{P}_{An}; \mathbf{P}_{Sm}) = \sigma_m \exp(-j2\pi f_c \tau_{nm}) \exp\left[j\pi f_{dr} (t - \tau_{nm})^2\right] \tag{4}$$

where, t is the fast time, f_c the carrier frequency, f_{dr} the LFM chirp rate, $\tau_{nm} = 2R(\mathbf{P}_{An}; \mathbf{P}_{Sm})/c$ the echo delay, and c the speed of light in vacuum.

After range focusing, the echo signal can be written as

$$S(r, \mathbf{P}_{An}; \mathbf{P}_{Sm}) = \sigma_m \chi_R \left(r - R(\mathbf{P}_{An}; \mathbf{P}_{Sm})\right) \exp(-j2kR(\mathbf{P}_{An}; \mathbf{P}_{Sm})) \tag{5}$$

where, r denotes the range domain, $k = 2\pi f_c/c$ the wave number, and $\chi_R(r - R(\mathbf{P}_{An}; \mathbf{P}_{Sm}))$ the range ambiguity function. For a multiple-scattering points observed scene, the received echo is the echo sum of all scatterers, i.e.,

$$S\left(r, \mathbf{P}_{An}\right) = \sum_{m \in \Omega} S(r, \mathbf{P}_{An}; \mathbf{P}_{Sm}) \tag{6}$$

Then we can parameterize Equation (6) in terms of the reflectivity vector $\boldsymbol{\sigma} \in \mathbb{C}^{M \times 1}$ and the delay-phase function $\boldsymbol{\psi}_n \in \mathbb{C}^{M \times 1}$ as follow:

$$S\left(r, \mathbf{P}_{An}\right) = \boldsymbol{\psi}_n\left(r\right)^T \boldsymbol{\sigma}, \quad n = 1, \ldots, N \tag{7}$$

where $\boldsymbol{\psi}_n(r) = [\chi_R(r - R(\mathbf{P}_{An}, \mathbf{P}_{Sm})) \exp(-j2\pi f_c \tau_{nm})]$ is interpreted as measurement vector of the nth APC at range r. We rearrange the echo signal Equation (7) to a vector as

$$\mathbf{S} = \left[S\left(r_i, \mathbf{P}_{An}\right)\right]^T, \quad i = 1, \ldots, P, \quad n = 1, \ldots, N \tag{8}$$

where $\mathbf{S}$ is an $NP \times 1$ vector and P the number of samples in range domain. If there are not phase error and noise, the relationship between $\boldsymbol{\sigma}$ and $\mathbf{S}$ can be compactly expressed as a linear model:

$$\mathbf{S} = \mathbf{A}\boldsymbol{\sigma} \tag{9}$$

where $\mathbf{A} \in \mathbb{C}^{NP \times M}$ denotes the SA-LASAR measurement matrix, and

$$\mathbf{A} = \left[\boldsymbol{\psi}_n\left(r_i\right)\right]^T, \quad n = 1, \ldots, N, \quad i = 1, \ldots, P \tag{10}$$

In practice, the sizes of $\mathbf{S}$, $\mathbf{A}$ and σ in Equation (10) are usually very large in SA-LASAR (e.g., to form a $1000 \times 1000 \times 1000$ medium size LASAR image, the length of vector $\boldsymbol{\sigma}$ will be 10^9 and the size of matrix $\mathbf{A}$ may be approximate $10^9 \times 10^9$), so it is both time consume and storage intensive to solve such a huge linear equation. To reduce the computational cost, we can divide the 3-D observed scene into a series of equiv-range 2-D slices [14], as shown in Figure 1(b), and deal with these slices separately. In this case, sparse recovery only affects on the APCs plane and the range focusing still depends on the classical MF.

Let $\Xi = \{1, 2, \ldots, M_s\}$ denotes the cell index set in each equiv-range slice, M_s denotes the number of the equiv-range slice cells. Obviously, compared to the whole 3-D observed space, we have $M_s \ll M$. In an equiv-range slice r_i, the coefficient vector $\mathbf{f}(r_i) \in \mathbb{C}^{M_s \times 1}$ and the measurement marix $\boldsymbol{\Phi}(r_i) \in \mathbb{C}^{P \times M_s}$ can simply be written as

$$\mathbf{f}(r_i) = \{f_w \,|f_w \in \mathbb{C}; w \in \Xi\}, \quad i = 1, \ldots, P \tag{11}$$

$$\boldsymbol{\Phi}(r_i) = [\psi_n(r_i)]^T, \quad n = 1, \ldots, N, \quad i = 1, \ldots, P \tag{12}$$

As a result, the echoes of the equiv-range slice r_i can be expressed as a linear expression

$$\mathbf{y}(r_i) = \boldsymbol{\Phi}(r_i)\,\mathbf{f}(r_i), \quad i = 1, \ldots, P \tag{13}$$

where

$$\mathbf{y}(r_i) = [S(r_i, \mathbf{P}_1), S(r_i, \mathbf{P}_2), \ldots, S(r_i, \mathbf{P}_N)]^T \tag{14}$$

2.2. Phase Errors of Observation Model

As mentioned in Section 1, there are various measurement errors during the SA-LASAR date collection, and these errors may cause additive phase errors in the echoes. Let $\boldsymbol{\phi}(r_i) \in \mathbb{R}^N$ denotes the phase error vector in the ith range slice r_i, and $\mathbf{R}(r_i) = \mathrm{diag}\{\exp(j\boldsymbol{\phi}(r_i))\}$ denotes the phase error matrix. The phase error corrupted data can be expressed as

$$\mathbf{y}_s(r_i) = \mathbf{R}(r_i)\,\mathbf{y}(r_i), \quad i = 1, \ldots, P \tag{15}$$

If we take an additive noise $\nu(r_i)$ into account (e.g., assuming white Gaussian noise), and submit Equation (13) into (15), the SA-LASAR signal model can be rewritten as a bilinear measurement model for the unknown reflectivity $\mathbf{f}(r_i)$ and phase error parameters $\mathbf{R}(r_i)$.

$$\mathbf{y}_s(r_i) = \mathbf{R}(r_i)\,\boldsymbol{\Phi}(r_i)\,\mathbf{f}(r_i) + \boldsymbol{\nu}(r_i), \quad i = 1, \ldots, P \tag{16}$$

Note that the linear model formulation in (16) is also applicable in the case of multiplicative noise (speckle), e.g., assume $\mathbf{S}(r_i)$ is the speckle noise matrix in range cell r_i, and then the measurement signal in (15) with speckle noise can be expressed as

$$\begin{aligned}\mathbf{y}_s\left(r_i\right)&=\mathbf{S}(r_i)\,\mathbf{R}(r_i)\mathbf{y}(r_i)=\mathbf{R}(r_i)\boldsymbol{\Phi}(r_i)\mathbf{f}(r_i)+\left[\mathbf{S}\left(r_i\right)-\mathbf{I}\right]\mathbf{R}\left(r_i\right)\boldsymbol{\Phi}(r_i)\mathbf{f}(r_i)\\&=\mathbf{R}\left(r_i\right)\boldsymbol{\Phi}\left(r_i\right)\mathbf{f}\left(r_i\right)+\boldsymbol{\nu}\left(r_i\right)\end{aligned}\tag{17}$$

where $\boldsymbol{\nu}(r_i) = [\mathbf{S}(\mathbf{r}_i) - \mathbf{I}]\mathbf{R}(r_i)\boldsymbol{\Phi}(r_i)\mathbf{f}(r_i)$ can be seen as an equivalent additive noise. For simplicity, here we only consider additive noise in the measurement signal.

In the case of phase errors, the aim of SA-LASAR imaging is to estimate $\mathbf{f}(r_i)$ and $\mathbf{R}(r_i)$ from the phase corrupted and noisy observed data $\mathbf{y}_s(r_i)$. For the sake of simplicity, we replace $\mathbf{y}_s(r_i)$, $\mathbf{f}(r_i)$, $\boldsymbol{\Phi}(r_i)$, $\mathbf{R}(r_i)$ and $\boldsymbol{\nu}(r_i)$ by $\mathbf{y}_s$, $\mathbf{f}$, $\boldsymbol{\Phi}$, $\mathbf{R}$ and $\boldsymbol{\nu}$ respectively in the following section.

3. SPARSE AUTOFOCUS RECOVERY FOR SA-LASAR

3.1. The Sparse Autofocus Recovery Approach

In one equiv-range slice, the LASAR image usually contains a few sparse scatterers. Based on this sparse spatial feature, we can employ CS-based sparse recovery approaches to reconstruct the SA-LASAR sparse reflectivity $\mathbf{f}(r_i)$ for all range slices. Numerical experiments have indicated that the ℓ_1-norm minimization regularization [31], i.e., iterative reweighted least square (IRLS) algorithm [32], performs exceptionally well in locating sparse solutions of underdetermined linear equations. Firstly we consider the phase error free case, i.e., $\mathbf{R} = \mathbf{I}$, the key feature of ℓ_1-norm reweighted regularization for Equation (16) is finding solution of a convex optimal problem

$$\hat{\mathbf{f}} = \arg\min_{f} J\left(\mathbf{f}\right)\tag{18}$$

where $J(\mathbf{f}) = \|\mathbf{W}\mathbf{f}\|_1 + \|\mathbf{y}_s - \boldsymbol{\Phi}\mathbf{f}\|_2$ is the objective function in SA-LASAR imaging without phase error, $\mathbf{W} = \mathrm{diag}(\boldsymbol{\omega})$, $\boldsymbol{\omega} = (\omega_1, \omega_1, \ldots \omega_{M_s})$ is the weights vector determined by the reflectivity $\mathbf{f}$. The theoretical analysis by [32] indicated the recovery error bound is tight under the weights

$$\omega_j = 1/(|f_j| + \xi), \quad j = 1, \ldots, M_s\tag{19}$$

where ξ is a small positive constant. Through ℓ_1-norm reweighted regularization, we can find a sparse solution to Equation (18) via iterative minimization as

$$\hat{\mathbf{f}}^{n+1} = \left(\boldsymbol{\Phi}^H\boldsymbol{\Phi} + \lambda_1^n\mathbf{W}^n\right)^{-1}\boldsymbol{\Phi}^H\mathbf{y}_s\tag{20}$$

where $\hat{\mathbf{f}}^{n+1}$ is the $n+1$th iterative recovered vector, λ_1^n the nth iterative regularization parameter and estimated by $\lambda_1^n = \|\mathbf{y}_s - \mathbf{\Phi}\hat{\mathbf{f}}^n\|_2/N$, and $\mathbf{W}^n = \mathrm{diag}(1/(|\hat{\mathbf{f}}^n| + \xi))$.

In this paper, our concern is different from the problem in (18) because we have to consider the phase errors $\mathbf{R} \neq \mathbf{I}$. For SA-LASAR sparse autofocus imaging, we aim to find the optimal solution of the following ill-conditioned constant modulus linear program (ICCMLP) problem.

$$\left(\hat{\mathbf{f}}, \hat{\mathbf{R}}\right) = \arg\min_{f,R} J\left(\mathbf{f}, \mathbf{R}\right) \text{ s.t } |\mathbf{R}_{ij}| = \begin{cases} 1 & i = j \\ 0 & i \neq j \end{cases}, \quad i, j = 1, \ldots, N \tag{21}$$

where $J(\mathbf{f}, \mathbf{R}) = \|\mathbf{W}\mathbf{f}\|_1 + \|y_s - \mathbf{R}\mathbf{\Phi}\mathbf{f}\|_2$ is the joint objective function of the unknown vector $\mathbf{f}$ and matrix $\mathbf{R}$. Because (21) is an NP-hard optimization problem, it is very difficult to find the optimal solution. Here, an iterative minimization via ℓ_1-norm reweights least square regularization autofocus algorithm is proposed to estimate the optimal solution of this ICCMLP problem. The algorithm can be divided into two convex optimization steps: reconstructing $\hat{\mathbf{f}}$ with fixed $\mathbf{R}$, and estimating $\hat{\mathbf{R}}$ with fixed $\mathbf{f}$. The update formulas of the method are displayed as follows:

(1) Suppose that we have obtained $\hat{\mathbf{f}}^n$, $\mathbf{W}^n$ and $\hat{\mathbf{R}}^n$ in the nth iteration, the vector $\hat{\mathbf{f}}$ is obtained by finding the solution of the following convex problem

$$\hat{\mathbf{f}}^{n+1} = \arg\min_{f} J\left(\mathbf{f} \,\middle|\, \hat{\mathbf{R}}^n\right) \tag{22}$$

where $J(\mathbf{f}|\hat{\mathbf{R}}^n) = \|\mathbf{f}\|_1 + \|\mathbf{y}_s - \hat{\mathbf{R}}^n\Phi\mathbf{f}\|_2$ is conditional objective function of $\mathbf{f}$ under $\hat{\mathbf{R}}^n$. Note that $\mathbf{R}^H = \mathrm{diag}(\exp(-j\boldsymbol{\phi}))$, and then $\mathbf{R}^H\mathbf{R} = \mathbf{I}$. According to Equation (20), we can use ℓ_1-norm based IRLS algorithm to estimate the optimal reflectivity vector $\hat{\mathbf{f}}^{n+1}$ as

$$\hat{\mathbf{f}}^{n+1} = \left(\mathbf{\Phi}^H\mathbf{\Phi} + \lambda_2^n\mathbf{W}^n\right)^{-1} \mathbf{\Phi}^H \left(\hat{\mathbf{R}}^n\right)^H \mathbf{y}_s \tag{23}$$

where

$$\lambda_2^n = \left\|\mathbf{y}_s - \hat{\mathbf{R}}^n\mathbf{\Phi}\hat{\mathbf{f}}^n\right\|_2 \Big/ N \tag{24}$$

(2) After estimating the reflectivity vector $\hat{\mathbf{f}}^{n+1}$, the following optimization needs to be solved

$$\hat{\mathbf{R}} = \arg\min_{R} J\left(\mathbf{R} \,\middle|\, \hat{\mathbf{f}}^{n+1}\right) \text{ s.t } |\mathbf{R}_{ij}| = \begin{cases} 1 & i = j \\ 0 & i \neq j \end{cases}, \quad i, j = 1, \ldots, N \tag{25}$$

where $J(\mathbf{R}|\hat{\mathbf{f}}^{n+1}) = \|\mathbf{y}_s - \mathbf{R}\boldsymbol{\Phi}\hat{\mathbf{f}}^{n+1}\|_2$. Substituting Equation (23) into Equation (16), we have

$$\left(\mathbf{I}-\boldsymbol{\Phi}\left(\boldsymbol{\Phi}^H\boldsymbol{\Phi}+\lambda_2^n\mathbf{W}^{n+1}\right)^{-1}\boldsymbol{\Phi}^H\right)\left(\hat{\mathbf{R}}^n\right)^H\mathbf{y}_s=\boldsymbol{\nu} \tag{26}$$

Let $\mathbf{Y} = \mathrm{diag}(\mathbf{y}_s)$, $\boldsymbol{\beta} = \exp(-j\boldsymbol{\phi})$, Equation (26) can be rewritten as

$$\left(\mathbf{I}-\boldsymbol{\Phi}\left(\boldsymbol{\Phi}i^H\boldsymbol{\Phi}+\lambda_2^n\mathbf{W}^{n+1}\right)^{-1}\boldsymbol{\Phi}^H\right)\mathbf{Y}\hat{\boldsymbol{\beta}}^n=\boldsymbol{\nu} \tag{27}$$

From Equation (27), we see that the phase error estimation is converted into finding a solution of the linear equation. If there is not noise in $\mathbf{y}_s$, i.e., $\boldsymbol{\nu} = 0$, phase errors can be exactly recovered by the direct calculation method, which was described in more detail in [29, 30]. However, when we consider the unknown noise $\boldsymbol{\nu} \neq 0$ and the estimation $\hat{\mathbf{f}}^{n+1}$ is not the exact solution, the direct calculation method may fail. Here, we solve Equation (27) by maximum likelihood estimation as

$$\hat{\boldsymbol{\beta}}_{opt}^{n+1}=\arg\min_{\beta}\left\|\left(\mathbf{I}-\boldsymbol{\Phi}\left(\boldsymbol{\Phi}^H\boldsymbol{\Phi}+\lambda_2^n\mathbf{W}^{n+1}\right)^{-1}\boldsymbol{\Phi}^H\right)\mathbf{Y}\boldsymbol{\beta}\right\|_2 \text{ s.t } |\beta_i| = 1, \\ i=1,\ldots,N \tag{28}$$

Note that (28) is a constant modulus quadratic program (CMQP) problem and it is also difficult to estimate the optimal resolution. Let $\mathbf{A} = (\mathbf{I} - \boldsymbol{\Phi}(\boldsymbol{\Phi}^H\boldsymbol{\Phi} + \lambda_2^{n+1}\mathbf{W}^n)^{-1}\boldsymbol{\Phi}^H)\mathbf{Y}$, $\mathbf{C} = \mathbf{A}^H\mathbf{A}$, $\mathbf{X} = \boldsymbol{\beta}\boldsymbol{\beta}^H$, because $\boldsymbol{\beta}^H\mathbf{C}\boldsymbol{\beta} = \mathrm{tr}(\boldsymbol{\beta}^H\mathbf{C}\boldsymbol{\beta}) = \mathrm{tr}(\mathbf{C}\boldsymbol{\beta}\boldsymbol{\beta}^H)$, the problem of Equation (28) can be formulated as a positive semi-definite matrices optimization program as

$$\begin{aligned}\hat{\mathbf{X}} &= \arg\min_X \mathrm{tr}\left(\mathbf{CX}\right) \text{ s.t } \mathbf{X} \succeq 0, \\ \mathrm{rank}\left(\mathbf{X}\right) &= 1, \quad \mathbf{X}_{ii} = 1, \quad i = 1,\ldots,N\end{aligned} \tag{29}$$

However, Equation (29) is a non-convex feasible set due to $\mathrm{rank}(\mathbf{X}) = 1$ constraint and cannot be solved efficiently. Instead, we relax the constraint $\mathrm{rank}(\mathbf{X}) = 1$ and have

$$\hat{\mathbf{X}} = \arg\min_X \mathrm{tr}\left(\mathbf{CX}\right) \text{ s.t } \quad \mathbf{X}\succeq 0, \quad \mathbf{X}_{ii} = 1, \quad i = 1,\ldots,N \tag{30}$$

Obviously, Equation (30) is a constrained quadratic convex optimization problem, which can be effectively solved by the standard convex optimization method, such as a state-of-the-art approximation method based on the semi-definite relaxation (SDR) program [33]. SDR can now be handled very conveniently and effectively by some readily available software packages, such as the convex optimization toolbox CVX [34]. After obtaining the SDR solution $\hat{\mathbf{X}}$ of Equation (30), if ank($\hat{\mathbf{X}}$) = 1, let $\hat{\mathbf{X}} = \hat{\boldsymbol{\beta}}\hat{\boldsymbol{\beta}}^H$, the optimal solution $\hat{\boldsymbol{\beta}}_{opt} = \hat{\boldsymbol{\beta}}$. Otherwise, let $\hat{\mathbf{X}} = \mathbf{B}\mathbf{B}^H$, where $\mathbf{B} = [\mathbf{b}_1, \mathbf{b}_2, \ldots, \mathbf{b}_l]$ is the square decomposed matrix of $\hat{\mathbf{X}}$, l may be larger than 1. In this case, the randomization method [35] is used to find the optimal solution $\hat{\boldsymbol{\beta}}_{opt}$ from $\mathbf{B}$. The randomization method generates M_r normally distributed complex vectors $\mathbf{u}_1, \mathbf{u}_2, \ldots, \mathbf{u}_{M_r}$ that are independent with zero mean and covariance $\mathbf{I}$. Let $\boldsymbol{\beta}_i = \exp(j\angle(\mathbf{B}\mathbf{u}_i))$, $i = 1, \ldots, M_r$, we can approximate the feasible solution $\hat{\boldsymbol{\beta}}_{opt}$ as

$$\hat{\boldsymbol{\beta}}_{opt}^{n+1} = \arg\min_{1\leq i\leq M_r} \|\mathbf{C}\boldsymbol{\beta}_i\|_2 \tag{31}$$

When the optimal solution $\hat{\boldsymbol{\beta}}_{opt}^{n+1}$ is obtained, the phase error matrix $\mathbf{R}$ is approximated as

$$\hat{\mathbf{R}}^{n+1} = \mathrm{diag}\left\{\left(\hat{\boldsymbol{\beta}}_{opt}^{n+1}\right)^H\right\} \tag{32}$$

Once $\|\mathbf{f}^{n+1} - \mathbf{f}^n\|_2 / \|\mathbf{f}^n\|_2 \leq \delta$ is satisfied, where δ is a small positive threshold, the iteration in steps (1) and (2) are finished. The steps involved for the proposed sparse autofocus recovery algorithm for SA-LASAR imaging are provided in Algorithm 1. For the matrix $\boldsymbol{\Phi}$ times an arbitrary vector, the complexity is $\mathcal{O}(NM_s)$. Hence, our approach will require approximate $\mathcal{O}(2\kappa NM_s^2)$ operations, where κ is the iteration number. However, we note that $\boldsymbol{\Phi}$ is a non-uniform fast Fourier transform (FFT) matrix. Therefore, the approach's complexity can be reduced to $\mathcal{O}(2\kappa NM_s \log M_s)$ by applying FFT optimization. Compare to the classical autofocus methods, the computational complexity of our approach is relatively large, but it performs very well in sparse scenarios involving under-sampled SA-LASAR data.

3.2. The Performance Metrics

To quantitatively evaluate the performance of our approach, three quality metrics are calculated: the normalized mean squared error (NMSE), the target-to-background ratio (TBR) and the entropy of image (ENT).

The NMSE is defined as

$$\mathrm{NMSE} = \left\|\hat{\mathbf{f}} - \mathbf{f}\right\|_2 \Big/ \|\mathbf{f}\|_2 \tag{33}$$

The TBR is defined as

$$\mathrm{TBR} = 20\log\left(N_B \max\nolimits_{i\in\mathbf{T}}\left(\left|\left(\hat{\mathbf{f}}\right)_i\right|\right) \Big/ \sum\nolimits_{j\in\mathbf{B}}\left(\left|\left(\hat{\mathbf{f}}\right)_j\right|\right)\right) \tag{34}$$

Algorithm 1. Sparse autofocus recovery for SA-LASAR imaging

```
Inputs: measurement matrix $\mathbf{\Phi}$, echo signal $\mathbf{y}_S$, threshold $\delta$, smooth parameter $\xi$.
Outputs: sparse reflectivity vector $\hat{\mathbf{f}}$, phase error matrix $\hat{\mathbf{R}}$.
Initialize: $\hat{\mathbf{R}}^0 = \mathbf{I}$, $\hat{\mathbf{f}}^0 = \mathbf{\Phi}^H \mathbf{y}_S$, $\mathbf{Y} = \text{diag}(\mathbf{y}_s)$, $n = 0$
while $\left\|\hat{\mathbf{f}}^{n+1} - \hat{\mathbf{f}}^n\right\|_2 \Big/ \left\|\hat{\mathbf{f}}^n\right\|_2 > \delta$ do
    1) Reconstruct $\hat{\mathbf{f}}$ from $\hat{\mathbf{f}} = \arg\min_f J\left(\mathbf{f}\left|\hat{\mathbf{R}}\right.\right)$ in (22) with fixed $\hat{\mathbf{R}}$
    $\mathbf{W}^n = \text{diag}\left(1 \Big/ \left(\left|\hat{\mathbf{f}}^n\right| + \xi\right)\right)$
    $\lambda_2^n = \left\|\mathbf{y}_s - \hat{\mathbf{R}}^n \mathbf{\Phi} \hat{\mathbf{f}}^n\right\|_2 \Big/ N$
    $\hat{\mathbf{f}}^{n+1} = \left(\mathbf{\Phi}^H \mathbf{\Phi} + \lambda_2^n \mathbf{W}^n\right)^{-1} \mathbf{\Phi}^H \left(\hat{\mathbf{R}}^n\right)^H \mathbf{y}_s$
    2) Estimate $\hat{\mathbf{R}}$ from (25) with fixed $\hat{\mathbf{f}}$
    $\mathbf{A} = \left(\mathbf{I} - \mathbf{\Phi}\left(\mathbf{\Phi}^H \mathbf{\Phi} + \lambda_2^{n+1} \mathbf{W}^{n+1}\right)^{-1} \mathbf{\Phi}^H\right) \mathbf{Y}$
    $\mathbf{C} = \mathbf{A}^H \mathbf{A}$
    $\hat{\mathbf{X}} = \arg\min_X \text{tr}\ (\mathbf{CX})$ s.t $\mathbf{X} \succ 0,\ \mathbf{X}_{ii} = 1,\ i = 1, \ldots, N$
    If rank $\left(\hat{\mathbf{X}}\right) = 1$, then $\hat{\mathbf{X}} = \hat{\boldsymbol{\beta}} \hat{\boldsymbol{\beta}}^H$, $\hat{\boldsymbol{\beta}}_{opt}^{n+1} = \hat{\boldsymbol{\beta}}$
    else using the randomization method to find the optimal solution
    $\hat{\mathbf{X}} = \mathbf{B}\mathbf{B}^H$
    $\hat{\boldsymbol{\beta}}_{opt}^{n+1} = \arg\min_{1 \le i \le M_r} \|\mathbf{C}\boldsymbol{\beta}_i\|_2$
    end If
    $\hat{\mathbf{R}}^{n+1} = \text{diag}\left\{\left(\hat{\boldsymbol{\beta}}_{opt}^{n+1}\right)^H\right\}$
    $n \leftarrow n + 1$
end while
return $\hat{\mathbf{f}} \leftarrow \hat{\mathbf{f}}^{n+1}$, $\hat{\mathbf{R}} \leftarrow \hat{\mathbf{R}}^{n+1}$
```

where $\mathbf{T}$ denotes the target region and is the background region, N_B is the number of pixels in the background region. A higher TBR value indicates that the target is easier to extract from its local background.

The ENT is defined as

$$\text{ENT} = -\sum_{i=1}^{G} \rho(i) \log_2 (\rho(i)) \tag{35}$$

where $\rho(i)$ denotes the gray level intensity histogram of the reconstructed vector $\hat{\mathbf{f}}$, G is the number of levels in the histogram. A smaller ENT value means a sharper image.

4. RESULTS

4.1. Simulated Data

The main parameters of the simulated data are listed in Table 1. The echoes are corrupted by complex Gaussian random noises with zeros-mean and different variances. And phase errors uniformly random distributed in $[-0.75\pi, 0.75\pi]$ are added in the echo data.

Table 1. The main parameters of the simulation.

The carrier frequency	$f_c = 30\,\mathrm{GHz}$	The scene center range	$R_0 = 1000\,\mathrm{m}$
The signal bandwidth	$B_r = 150\,\mathrm{MHz}$	The real aperture length	$D_a = 2.5\,\mathrm{m}$
The LAA length	$L_A = 8\,\mathrm{m}$	The LAA element number	$N_A = 400$
Range Sample number	$N_r = 128$	Azimuth sample number	$N_s = 128$

As PGA method is the most widely used autofocus method in SAR imaging, we compare our algorithm with PGA to confirm its performance. Figure 2 shows the imaging results of the simulated data with a SNR = 20 dB. The original synthetic scene is a ship SAR image from European Remote Sensing (ERS) satellite. The size of each image is 40 × 40 with the width 50 m × 50 m. From Figure 2, both MF and MF-PGA obviously suffer from high sidelobes with the sparse LAA. In addition, without the phase errors, IRLS performs well. But if there are phase errors, IRLS suffers from serious image defocus. Although PGA can improve IRLS image quality, there are still many artifacts in the background. Obviously, the presented method can effectively suppress the artifacts, and provides a better image quality than PGA autofocus. But we also note that there are still some low artifacts in our approach's result due to the small residual between the estimated phase errors and the original phase errors.

The quantitative metrics for the reconstruction of the scene in Figure 2 via SNRs are plotted in Figure 3. From these results, it is also clearly seen that the proposed algorithm produces the best results in terms of the MSE, TBR and ENT metric, which means that

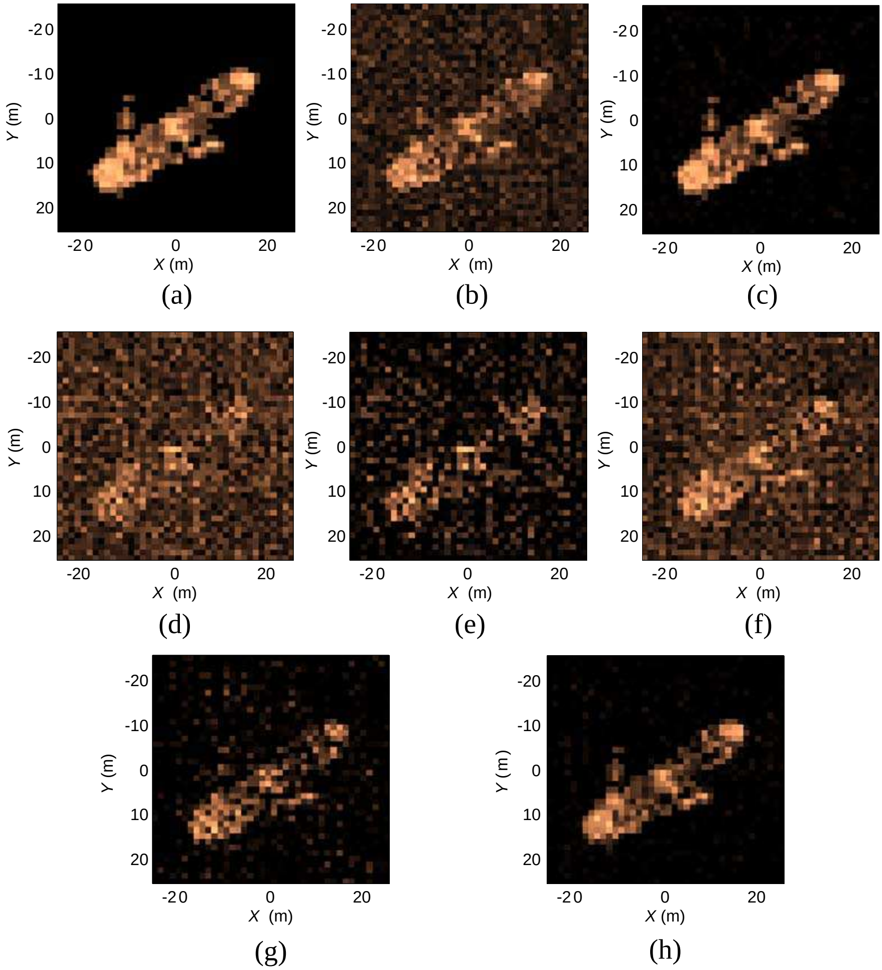

(a) (b) (c) (d) (e) (f) (g) (h)

Figure 2. Reconstructed results by different methods. (a) The original scene. (b) MF without phase errors. (c) IRLS without phase errors. (d) MF. (e) IRLS. (f) MF-PGA. (g) IRLS-PGA. (h) The proposed method.

it performs much better than the conventional PGA autofocus. To compare the computation times, these algorithms were implemented using non-optimized Matlab code on an Intel Core 2.2 GHz CPU. The computation times required by MF, MF-PGA, IRLS, IRLS-PGA and the proposed method are 0.24, 2.28, 74.12, 77.58 and 128.42 s, respectively. Hence, our approach requires more computational

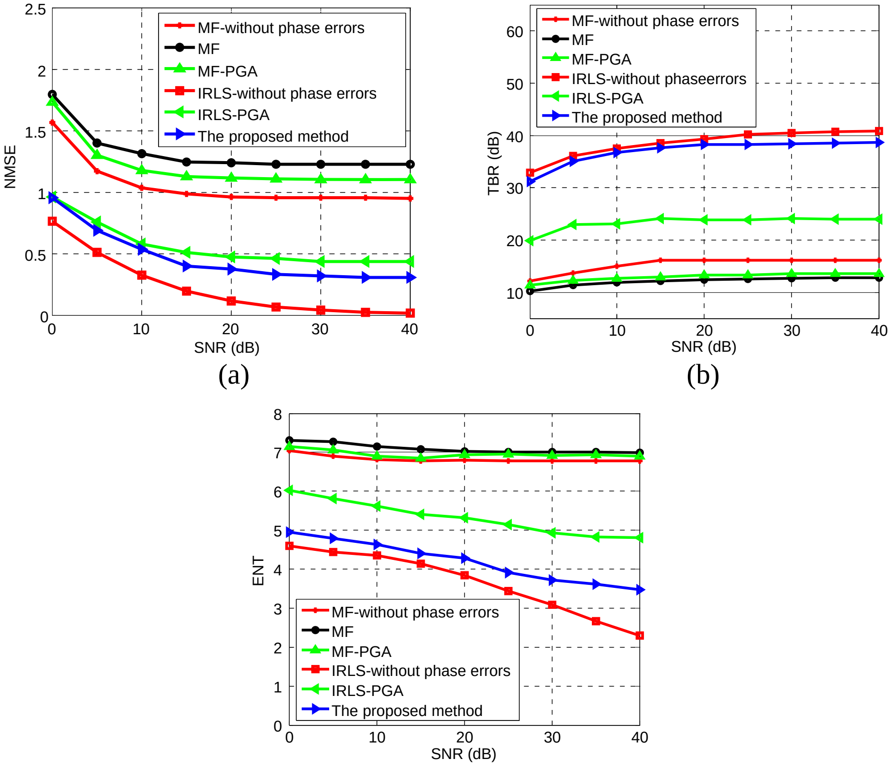

(a) (b)

(c)

Figure 3. Performance metrics via different SNRs. (a) NMSE. (b) TBR. (c) ENT.

complexity than conventional PGA autofocus methods, especially for the large date processing. However, with the rapid advances in signal processor hardware, its fast implementation is feasible.

4.2. Experimental Data

Two real experiments are demonstrated in this section. The experimental data is obtained by the ground-based SA-LASAR system developed by UESTC [4, 12–14]. Figure 4 shows the ground-based experimental system and the two tested targets. The main system parameters are displayed as follows: the carrier frequency $f_c = 9.62\,\mathrm{GHz}$, the signal bandwidth $B_r = 120\,\mathrm{MHz}$, the LAA length $L_A = 1.25\,\mathrm{m}$. In each azimuth cell, only sparse $N = 50$ virtual elements are active. In both experiments, the assist motion measurement data is never used. Because the speeds of the motion sensors are supposed to be constant, but in practice these speeds may change during different PRIs. Hence the phase errors caused by speed uncertainty in this system cannot be ignored and must be corrected.

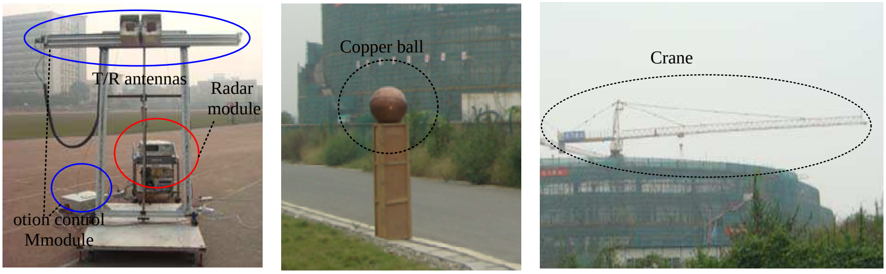

(a) (b) (c)

Figure 4. The ground-based LASAR system and the tested targets. 3-D imaging results of the copper ball. (a) The experimental system. (b) The copper ball. (c) The crane.

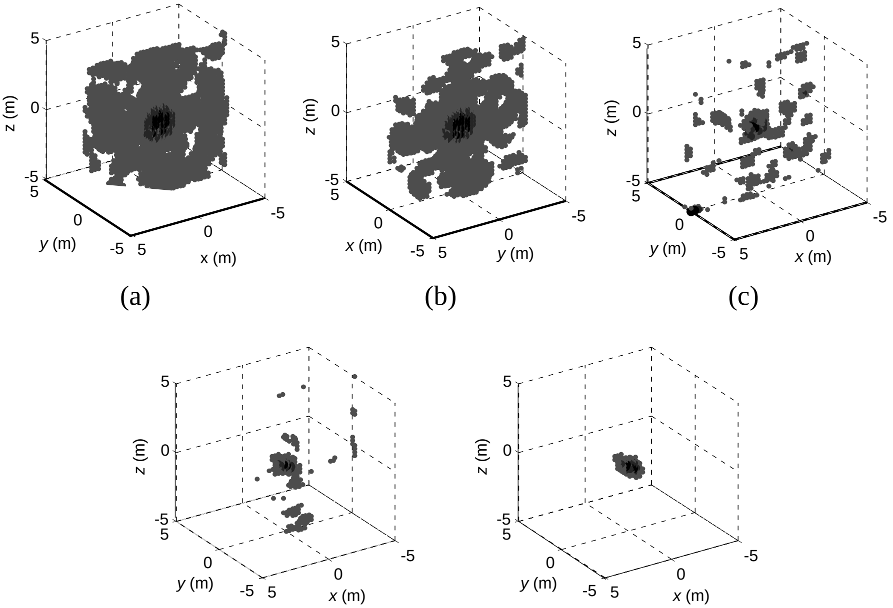

(d) (e)

Figure 5. The 3-D imaging results of the copper ball. (a) MF. (b) MF-PGA. (c) IRLS. (d) IRLS-PGA. (e) The proposed method.

In the first experiment, the observed scene consists of only one copper ball. Its distance to the sensor is about $R = 100\,\mathrm{m}$. The top 25 dB magnitude voxels of recovered images by MF, MF-PGA, IRLS, IRLS-PGA and the proposed method are respectively displayed in Figure 5. The deeper color means the stronger reflectivity. The size of these images is $41 \times 41 \times 41$ with each cell is $0.25\,\mathrm{m} \times 0.25\,\mathrm{m} \times 0.25\,\mathrm{m}$. As seen in Figure 5, conventional MF and MF-PGA images suffer from high sidelobe and low resolution due to the limited length under-sampled LAA. On the other hand, IRLS also suffers from serious artifacts because the inaccurate model with phase errors interference. Though IRLS-PGA provides better image than that IRLS, some artifacts still appear in background areas. Clearly, the proposed method outperforms the other methods, and provides high-quality image with enhanced feature at high resolution, low sidelobes and reduced number of artifacts.

In the second experiment, the scene is a crane. The length of the crane is about 50 m. The range from the crane to the SA-LASAR sensor is 160 m. Figure 6 shows the 3-D recovered images of the crane by the different methods. Also, the top 25 dB magnitude pixels are

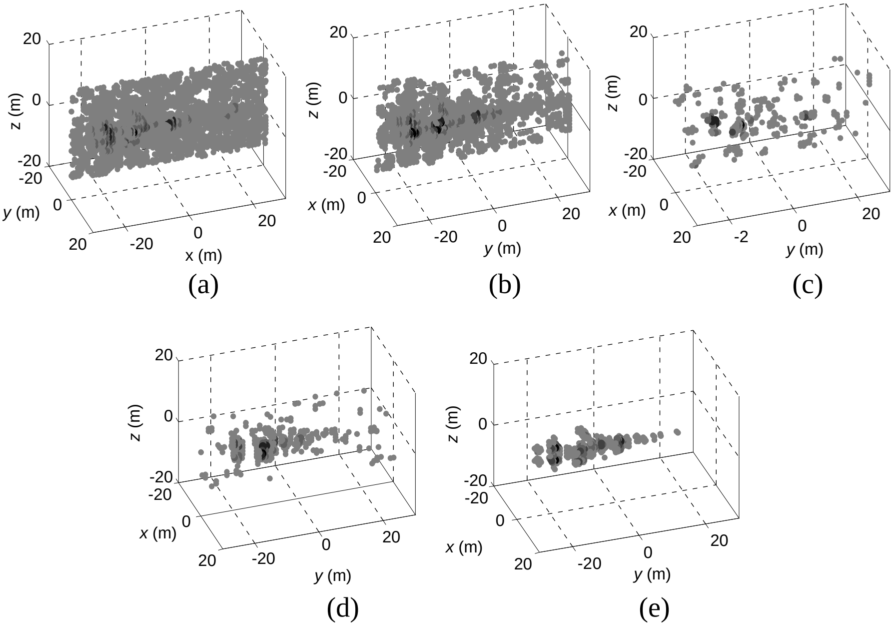

(a) (b) (c)

(d) (e)

Figure 6. The 3-D imaging results of the crane. (a) MF. (b) MF-PGA. (c) IRLS. (d) IRLS-PGA. (e) The proposed method.

displayed. The size of these 3-D images are 61 × 31 × 31 with each pixel is 1 m × 1 m × 1 m. From these results, we see that the proposed method can clearly capture the main features of the crane, and produce lower sidelobes and fewer artifacts in the background regions than the MF and IRLS with PGA autofocus.

The quantitative evaluation of the both experiments with TBR and ENT is given in Table 2. We find that the proposed method provides higher TBR and lower ENT than MF and IRLS with PGA autofocus, which means that our method improves the quality of reconstructed image and obtains a sharper image.

Table 2. Evaluation results of the experiments.

Methods	Ball		Crane	
	TBR	ENT	TBR	ENT
MF	28.11	4.701	24.81	5.198
MF-PGA	29.98	4.542	27.48	4.724
IRLS	44.47	1.467	49.65	1.245
IRLS-PGA	48.81	1.213	51.10	0.829
The proposed method	**54.12**	**0.622**	**56.68**	**0.675**

5. CONCLUSIONS

In this paper, we present a sparse autofocus recovery approach based on compressed sensing to obtain high quality SA-LASAR 3-D images with under-sampled and phase error corrupted data. Joint the bilinear expression models of both unknown phase errors and reflectivity image, the SA-LASAR 3-D image is reconstructed by exploiting the prior sparsity of observed scene. In the scheme, the approach involves solving the two optimization problems by the ℓ_1-norm reweight regularization and the semi-definite relax program respectively. Simulated and Experimental results show that the approach works effectively for SA-LASAR 3-D image formation in the case of sparse LAA and phase errors interference.

ACKNOWLEDGMENT

This work was supported by the Fundamental Research Funds for the Central Universities (No. E022050205), the Doctoral Fund of Ministry of Education of China (No. 20110185110001) and the China Scholarship Council Program (No. 2011607061). The authors thank the anonymous reviewers for their valuable comments to improve the paper quality.

REFERENCES

1. Klare, J., A. Brenner, and J. Ender, "A new airborne radar for 3D imaging-image formation using the ARTINO principle," *6th European Conference on Synthetic Aperture Radar*, 1–4, 2006.
2. Weiß, B. M., O. Peters, and J. Ender, "First flight trials with ARTINO," *7th European Conference on Synthetic Aperture Radar*, Vol. 4, 187–190, 2008.
3. Weiß, M. and M. Gilles, "Initial ARTINO radar experiments," *8th European Conference on Synthetic Aperture Radar*, 7–10, 2010.
4. Shi, J., X.-L. Zhang, et al., "APC trajectory design for 'one-active' linear-array three-dimensional imaging SAR," *IEEE Transactions on Geoscience and Remote Sensing*, Vol. 48, No. 3, 1470–1486, 2010.
5. Peng, X., W. Tan, Y. Wang, W. Hong, and Y. Wu, "Convolution back-projection imaging algorithm for downward-looking sparse linear array three dimensional synthetic aperture radar," *Progress In Electromagnetics Research*, Vol. 129, 287–313, 2012.
6. Wu, J., J. Yang, Y. Huang, Z. Liu, and H. Yang, "A new look at the point target reference spectrum for bistatic SAR," *Progress In Electromagnetics Research*, Vol. 119, 363–379, 2011.
7. Xu, H., J. Gao, and J. Li, "A variable PRF imaging method for high squint diving SAR," *Progress In Electromagnetics Research*, Vol. 135, 215–229, 2013.
8. Mahafza, B. R. and M. Sajjadi, "Three-dimensional SAR imaging using linear array in transverse motion," *IEEE Trans. Aerospace and Electronic Systems*, Vol. 32, No. 1, 499–510, Jan. 1996.
9. Ender, J. H. G. and J. Klare, "System architectures and algorithms for radar imaging by MIMO-SAR," *IEEE Radar Conference*, 1–6, 2009.
10. Huang, Y., P. V. Brennan, D. Patrick, I. Weller, P. Roberts, and K. Hughes, "FMCW based MIMO imaging radar for maritime navigation," *Progress In Electromagnetics Research*, Vol. 115, 327–342, 2011.
11. Zhou, W., J.-T. Wang, H. W. Chen, and X. Li, "Signal model and moving target detection based on MIMO synthetic aperture radar," *Progress In Electromagnetics Research*, Vol. 131, 311–329, 2012.

12. Shi, J., X. L. Zhang, J. Yang, and K. Liao, "Experiment results on one-active LASAR," *IEEE Radar Conference*, 1–4, 2009.
13. Shi, J., K.-F. Liao, and X.-L. Zhang, "Three-dimensional SAR with fixed transmitter and its scattering explanation," *Progress In Electromagnetics Research*, Vol. 133, 285–307, 2013.
14. Wei, S.-J., X.-L. Zhang, J. Shi, and K.-F. Liao, "Sparse array microwave 3-D imaging: Compressed sensing recovery and experimental study," *Progress In Electromagnetics Research*, Vol. 135, 161–181, 2013.
15. Herman, M. and A. Strohmer, "High-resolution radar via compressed sensing," *IEEE Transactions on Signal Processing*, Vol. 57, No. 6, 2275–2284, 2009.
16. Migliore, M. D., "A compressed sensing approach for array diagnosis from a small set of near-field measurements," *IEEE Transactions on Antennas and Propagation*, Vol. 59, No. 6, 2127–2133, 2011.
17. Liu, Z., X. Wei, and X. Li, "Adaptive clutter suppression for airborne random pulse repetition interval radar based on compressed sensing," *Progress In Electromagnetics Research*, Vol. 128, 291–311, 2012.
18. Poli, L., G. Oliveri, and A. Massa, "Microwave imaging within the first-order born approximation by means of the contrast-field bayesian compressive sensing," *IEEE Transactions on Antennas and Propagation*, Vol. 60, No. 6, 2865–2879, 2012.
19. Wang, Y., Q. Song, T. Jin, Y. Shi, and X.-T. Huang, "Sparse time-frequency representation based feature extraction method for landmine discrimination," *Progress In Electromagnetics Research*, Vol. 133, 459–475, 2013.
20. Patel, V. M., G. R. Easley, and D. M. Healy, "Compressed synthetic aperture radar," *IEEE Journal of Selected Topics in Signal Processing*, Vol. 4, No. 2, 244–254, 2010.
21. Wei, S.-J., X.-L. Zhang, J. Shi, and G. Xiang, "Sparse reconstruction for SAR imaging based on compressed sensing," *Progress In Electromagnetics Research*, Vol. 109, 63–81, 2010.
22. Roberts, W., J. Li, and P. Stoica, "Sparse learning via iterative minimization with application to MIMO radar imaging," *IEEE Transactions on Signal Processing*, Vol. 59, No. 3, 1088–1101, 2011.
23. Zhu, X.-X. and R. Bamler, "Tomographic SAR inversion by ℓ_1-norm regularization the compressive sensing approach," *IEEE Transactions on Geoscience and Remote Sensing*, Vol. 48, No. 10,

3839–3846, 2010.

24. Chen, J., J. Gao, Y. Zhu, W. Yang, and P. Wang, "A novel image formation algorithm for high-resolution wide-swath spaceborne SAR using compressed sensing on azimuth displacement phase center antenna," *Progress In Electromagnetics Research*, Vol. 125, 527–543, 2012.
25. Wei, S.-J., X.-L. Zhang, and J. Shi, "Linear array SAR imaging via compressed sensing," *Progress In Electromagnetics Research*, Vol. 117, 299–319, 2011.
26. Wahl, D. E., P. H. Eichel, D. C. Ghiglia, et al., "Phase gradient autofocus — A robust tool for high resolution SAR phase correction," *IEEE Trans. Aerospace and Electronic Systems*, Vol. 30, No. 3, 827–835, 1994.
27. Morrison, R. L., M. N. Do, and D. C. Munson, "MCA: A multichannel approach to SAR autofocus," *IEEE Trans. Image Process.*, Vol. 18, No. 4, 840–853, 2009.
28. Liu, K.-H., A. Wiesel, and D. C. Munson, "Synthetic aperture radar autofocus based on a bilinear model," *IEEE Trans. Image Process.*, Vol. 21, No. 5, 2735–2746, 2012.
29. Onhon, N. O. and M. A. Çetin, "Sparsity-driven approach for joint SAR imaging and phase error correction," *IEEE Trans. Image Process.*, Vol. 21, No. 4, 2075–2088, 2012.
30. Uğur, S. and O. Arıkan, "SAR image reconstruction and autofocus by compressed sensing," *Digital Signal Processing*, Vol. 22, No. 6, 923–932, 2012.
31. Fornasier, M. and H. Rauhut, "Compressive sensing," Vol. 1, 187–229, *Handbook of Mathematical Methods in Imaging,* Springer, 2010.
32. Zhao, Y. B. and D. Li, "Reweighted ℓ_1-minimization for sparse solutions to underdetermined linear systems," *SIAM Journal on Optimization*, Vol. 22, No. 3, 1065–1088, 2012.
33. Luo, Z. Q., W. K. Ma, A. M. Cho, et al., "Semidefinite relaxation of quadratic optimization problems," *IEEE Signal Processing Magazine*, Vol. 27, No. 3, 20–34, 2010.
34. Grant, M., S. Boyd, and Y. Ye, "CVX users' guide," Available Online at: http://cvxr.com/cvx/doc, Accessed Dec. 10, 2012.
35. So, M., J. Zhang, and Y. Ye, "On approximating complex quadratic optimization problems via semidefinite programming relaxations," *Mathematical Programming*, Vol. 110, No. 1, 93–110, 2007.